ACS OMEGA

http://pubs.acs.org/journal/acsodf

Article

Novel Amorphous Carbons for the Adsorption of Phosphate: Part I. Elucidation of Chemical Structure of N-Metal-Doped Chars

Michael Ayiania, Aidan Garcia, Sohrab Haghighi Mood, Jean-Sabin McEwen,* and Manuel Garcia-Perez*

Cite This: *ACS Omega* 2022, 7, 14490−14504

Read Online

ACCESS | Metrics & More | Article Recommendations

ABSTRACT: Due to phosphate's necessity in agriculture and its danger to the environment, the development of adsorbents for its removal has been the subject of intensive research activity. Although the introduction of nitrogen functionality to chars and modification of biochar with metals have proven to change the character of the char structure, making it more active toward nutrients, there is no study regarding the doping of biochar with metals and nitrogen simultaneously for the adsorption of phosphates. This paper is the first of two in which we report the production, characterization, and evaluation of N-metal-doped biochars from cellulose for phosphate removal from liquid effluents. In this part, we describe the production and characterization of N-Ca-, N-Fe-, and N-Mg-doped biochars. The elemental composition and surface area of each of the materials produced is reported. Elemental and surface characterization of the chars are reported with the largest N content appearing at a temperature of 800 °C (12.5 wt %) and a maximum surface area for biochar produced at 900 °C (1314 m^2/g). All of the adsorbents were visualized by scanning electron microscope (SEM), confirming that although there are some crystals on the surface of the biochar produced, most of the N, Mg, and Ca are part of the polyaromatic ring structure. Transmission electron microscope (TEM) images clearly show the formation of nanoclusters with the metals in the case of N-Fe and N-Ca biochars. The N-Mg biochars show a uniform distribution of the Mg through the carbon surface. X-ray photoelectron spectroscopy (XPS) studies of the biochars produced with metals and varying nitrogen levels clearly show Mg and Ca peaks shifting their position in the presence of N, suggesting the formation of stable structures between metals and N in the carbon polyaromatic ring system. To elucidate the nature of these structures, we conducted DFT-based calculations on different configurations of the nitrogenated structures. The calculated binding energy shifts were found to closely match the XPS experimental binding energy, confirming the likelihood of these structures in biochar. Finally, based on our experimental and modeling results, we hypothesize that an important fraction of the Mg and Ca is introduced to these biochars at the edges. Another fraction of Mg and Ca is in the form of phthalocyanine-like internal structures. More experimental studies are needed to confirm the formation of these very interesting structures and their potential use as adsorbents or catalysts.

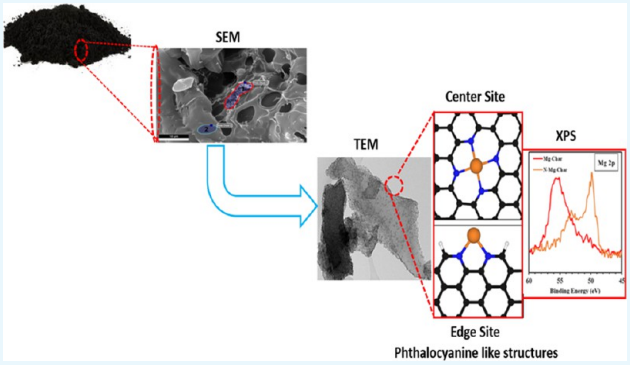

1. INTRODUCTION

Nitrogenated carbon materials are of recent interest due to their excellent properties in a variety of applications, such as carbon electrodes[1] and heterogeneous catalysis.[2−5] There are also several studies where nitrogenated carbons show efficient adsorption capacities toward pollutants[6−9] and good performance in batteries.[10−12] Phosphate is essential for modern agriculture but is a dangerous pollutant when released into the environment. While uncontrolled nutrient disposal in water bodies results in dead zones and eutrophication, adsorbents such as biochar have shown promise in controlling these pollutants.[13−16] Previous studies show that biochar does not perform well for the removal of phosphate without modification[17−19] but is suitable for the removal of several pollutants from wastewater when metals are added. In other studies, the introduction of nitrogen functionality to chars has proven to characteristically change its structure, making it more active toward foreign molecules such as metals and nutrients.[20] In spite of the promising characteristics of both modifications, there is a limited number of studies with regard to the doping of biochar with metals as well as nitrogen.

Received: October 12, 2021
Accepted: March 17, 2022
Published: April 22, 2022

© 2022 The Authors. Published by American Chemical Society

Understanding the chemical nature of the metal in N-doped biochar, whether the metal is in the form of nanocrystals on the surface of the biochar or embedded in the matrix of the carbon materials, is critical to designing better adsorbents. Hence, the main goal of this paper is to produce and characterize N-metal-doped biochar. In the second part, the capacity of biochars doped with nitrogen and metals with regard to phosphate adsorption is evaluated.

2. METHODS AND MATERIALS

2.1. Sample Preparation. Magnesium chloride hexahydrate ($MgCl_2 \cdot 6H_2O$), calcium chloride ($CaCl_2$), and iron (III) chloride ($FeCl_3$) were purchased from Sigma-Aldrich to prepare the solutions and pretreat the feedstocks. All solutions used in this work were prepared with deionized (DI) water, which was also used to rinse and clean the samples. Briefly, 5 wt % solution was prepared, and each feedstock was immersed into the solution for 1 h. The mixture of biomass and solution was then oven-dried 24 h at 105 °C to remove the water.

2.2. Nitrogen-Metal-Doped Biochar Production. To better control the structure of the resulting biochar, Avicel cellulose was used as a starting material. N-doped biochars were produced using ammonia through a one-step ammonization process at five different temperatures (500, 600, 700, 800, 900 °C). This was conducted in a Quartz Tube furnace reactor with 50 mm OD by 44 mm ID at a length of 1.0 m. Briefly, cellulose was kept in a tubular furnace in contact with N_2 for 30 min at 25 °C. Then, the temperature was increased from 25 °C to the desired set temperature at a heating rate of 10 °C min^{-1} under an ammonia environment. When the final temperature is reached, the sample is allowed a residence time of 30 min in the reactor. A flow rate of 1000 mL min^{-1} for ammonia was employed. The final biochar produced was cooled down to 25 °C at the same rate before storage and characterization.

Nitrogen-metal biochars were also produced using avicel cellulose and three different metals, but all of these studies were conducted at 800 °C (at this temperature, we obtained the highest incorporation of nitrogen). Solutions of 5 wt % Mg, Ca, and Fe were prepared from $MgCl_2$, $CaCl_2$, and $FeCl_3$, respectively, and later mixed with cellulose in a ratio of 2.8:1 (Solution/Cellulose). The cellulose was fully covered with the solution to ensure uniform distribution. The mixtures were then oven-dried for 24 h. Figure 1 is a block diagram outlining the course of the methodology and the manuscript.

2.3. Elemental Analysis. Elemental analysis was performed using a TruSpec-CHN elemental analyzer (LECO). Briefly, 0.15 g of the sample was used to determine total carbon (C), nitrogen (N), and hydrogen (H) contents. Oxygen (O) mass fraction was determined by subtracting the ash, C, N, and H contents from the total mass of the sample.

2.4. Proximate Analysis. Moisture, fixed carbon, volatile matter, and ash content in all biochars produced were determined using a thermogravimetric analyzer, SDTA851e (Mettler Toledo). The percentage of fixed carbon was determined by subtracting the ash percentage from the volatile matter percentage after assigning all weight loss up to 120 °C to loss of free and non-structural water. Briefly, moisture content was measured as the weight loss after the char was heated in a crucible from 25 to 120 °C and held at this temperature for 3 min under a nitrogen gas environment at a flow rate of 50 mL/min. Then, the char was heated from 120 to 950 °C under a nitrogen gas environment to determine volatile content. It was then held at this temperature for 5 min and cooled down to 450 °C. Ash was determined after heating the char from 450 to 600 °C under oxygen gas flow (50 mL/min).

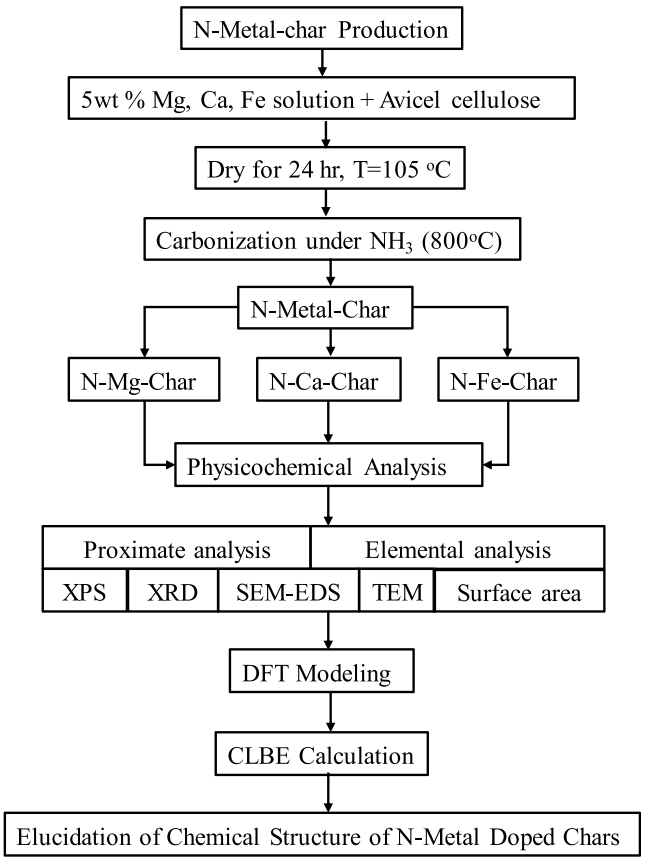

Figure 1. Schematic representation of tasks described in this paper.

2.5. Gas Physisorption Analysis for Biochar Surface Area and Porosity. Carbon dioxide (CO_2) and nitrogen adsorption isotherms were measured at 273 and 77 K, respectively, on micromeritics TriStar II PLUS surface area and porosity analyzer (Norcross, GA). Before each analysis, biochar samples were degassed at 250 °C for 18 h under a vacuum of 0.05−0.1 mbar (the degassing temperature was chosen based on the production temperature of the biochar to avoid sample degradation during preparation). CO_2 adsorption isotherms were measured between the partial pressure range of $P/P_o = 10^{-5}$ to $P/P_o = 0.03$ using 75 set equilibration points, and nitrogen isotherms were measured between $P/P_o = 10^{-5}$ to 0.99 and desorption between $P/P_o = 0.99$ to 0.01, where the relative pressure (P/P_o) is the ratio of absolute gas pressure to saturation pressure. The saturation pressure of N_2 at 77 K is 101.3 kPa[21] while the surface area, and micropore volumes were estimated for CO_2 and N_2 adsorption using the Dubinin−Radushkevich (DR) equation and BET model, respectively.[22,23]

2.6. SEM and TEM. Scanning electron micrographs of all chars were collected using an Apreo VolumeScope equipped with a field emission gun electron source. All samples were prepared by coating with 3 nm of gold to enhance resolution using a Cressington Hi-Res Sputter Coater. The images were collected under vacuum with a chamber pressure below 10 mPa. The accelerating voltage was set at 30 kV for all samples.

https://doi.org/10.1021/acsomega.1c05718
ACS Omega 2022, 7, 14490−14504

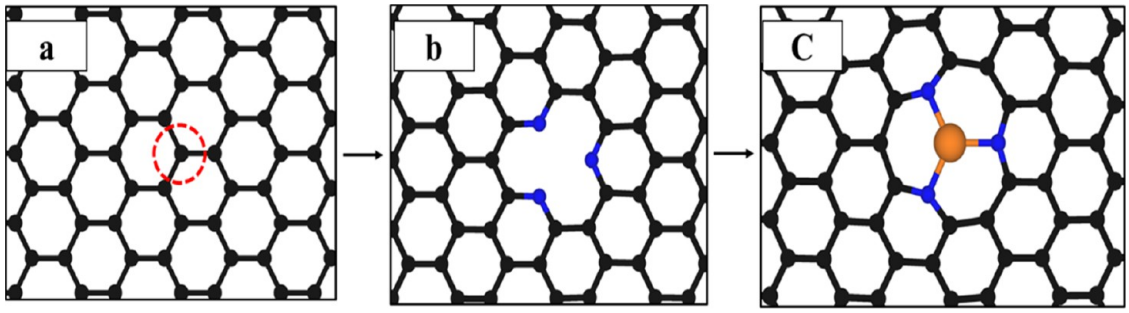

Figure 2. Schematic representation of the creation of the N-metal graphene models, where (a) is the creation of a single point defect. (b) Introduction of nitrogen to replace the dangling carbon forming pyridinic groups. (c) Metal atom is embedded in the matrix of the graphene. The black, orange, and blue spheres represent carbon, magnesium, and nitrogen atoms, respectively.

Specimens for the transmission electron microscope (TEM) study were prepared by grinding the biochar into a fine powder. A suspension of DI water and the powdered biochar were prepared and deposited onto copper grids. Imaging was carried out at 200 kV and under vacuum conditions with a FEI Tecnai G2 20 Twin. Care was taken to minimize exposure to a focused electron beam to avoid specimen damage.

2.7. X-Ray Photoelectron Spectroscopy. Analysis using XPS was performed using an AXIS-165 upgraded to an Ultra manufactured by Kratos Analytical Inc. Achromatic X-ray radiation of 1253.6 eV (MgKα) was used to analyze each material. All high-resolution spectra were recorded using a pass energy of 40 eV and a spot size of approximately 120 μm. The spectrometer was calibrated against both the Au $4f_{7/2}$ peak at 84.0 eV and the Ag $3d_{5/2}$ peak at 368.3 eV. The minimum full width at half maximum (FWHM) for the Au $4f_{7/2}$ peak is approximately 0.85 eV, representing the absolute minimum possible broadness achievable for this configuration. Survey scans have been obtained using a pass energy of 80 eV and step sizes of 1 eV to determine the overall chemical composition of each sample. To determine the speciation of carbon, nitrogen, and oxygen groups, high-resolution scans of the C 1*s*, N 1*s*, O 1*s*, and Mg 2*p* regions (280−295, 394−404, 527−538, and 45−60 eV, respectively) were collected for each material using 0.1 eV step sizes.

2.8. X-ray Powder Diffraction (XRD). X-ray diffraction (XRD) analysis was conducted to identify crystallographic structures in the biochar samples using a Rigaku (Miniflex 600) with Cu K α radiation operated at 40 kV, 15 mA in steps of 0.01°, with a scanning rate at 0.5 ° min^{-1} from 10 to 100°.

2.9. Computational Calculations. To better understand the effect of nitrogen functionality and metals (Mg/Ca), we computationally quantified the stability of Mg/Ca centers supported by various types of nitrogen functional groups. Using the energies generated computationally, adsorption energies for magnesium and calcium were calculated using the following equation

$$E_{ads} = E_{Mg/Ca_{ads}} - (E_{surf} + E_{Mg_{bulk}/Ca_{bulk}}) \quad (1)$$

where E_{ads} denotes the calculated adsorption energy, ($E_{Mg/Ca_{ads}}$), the energy of the entire surface-Mg/Ca structure, E_{surf} the energy of the functionalized carbon surface, and ($E_{Mg_{bulk}/Ca_{bulk}}$), the calculated energy of the bulk material. We have further quantified the adsorption energy of water on N-Mg-doped graphene and quantified the adsorption strength of water using

$$E_{ads}^{H_2O} = E_{H_2O/Mg} - (E_{Mg_{ads}} + E_{H_2O(g)}) \quad (2)$$

where $E_{ads}^{H_2O}$ denotes the adsorption energy of water on the N-Mg-doped structure, $E_{Mg_{ads}}$, the energy of the entire surface-Mg structure, and $E_{H_2O(g)}$, the energy of the water molecule in the gas phase. DFT calculations were carried out using the Vienna *Ab initio* Simulation Package (VASP).[24−26] The projector-augmented wave (PAW) method[27,28] was used to model the core electrons (POTCARs released in 2002 for C, and N and 2001 for H, Mg, and 2000 for Ca), and a plane-wave basis set with an energy cutoff of 450 eV was used to model the valence electrons. To model the electron exchange and correlation, the Perdew−Burke−Ernzerhof (PBE) functional[29] was applied (POTCAR set updated 2007). The Gaussian smearing method was used to set partial occupancies of bands with a smearing width of 0.2 eV to facilitate Brillouin zone integration convergence, followed by extrapolation to zero Kelvin for the total energy calculation.[30,31] All ground state optimizations used the conjugate gradient method and were considered converged when the relaxed interatomic cartesian forces were smaller than 0.025 eV/Å. The SCF energy tolerance was set to 10^{-5} eV. Spin polarization was also used for all calculations to account for any magnetization. Calculations for bulk Mg were optimized to confirm a simple hexagonal cell with a lattice constant 3.19 Å and an a/c ratio of 1.624 using a (10 × 10 × 10) Monkhorst−Pack grid. Bulk Ca was optimized in the same fashion to obtain a face-centered cubic cell with a lattice constant of 5.68 Å. Nitrogen and metal functionalization was studied in a graphene nanoribbon within a hydrogen-terminated edge model with dimensions of (29 × 17 × 21 Å). These ribbons allow for edge site adsorption and were used across all tested structures to provide comparable results. The graphene lattice constant was 2.467 Å, consistent with previous results.[32−34] The integration of the Brillouin zone was conducted using a (1 × 2 × 3) Monkhorst−Pack grid. All structures were visualized using VESTA[35]

Figure 2 shows the strategy used to generate the model of N-metal-doped biochar structures for our DFT calculations. We proposed various structural configurations of nitrogen and metal (Mg/Ca) based on our experimental results and calculated the stability and the core-level binding energy shifts (CLBES) of these structures.

The structure with metal atoms at the center of the pyridine-nitrogen or the pyrrolic-nitrogen in graphene was created through two steps: (i) the creation of a pyridine-nitrogen/pyrrolic-nitrogen, the substitution of under-coordinated carbons by N atoms to form a single vacancy or di-vacancy,

https://doi.org/10.1021/acsomega.1c05718
ACS Omega 2022, 7, 14490−14504

Table 1. Char Yield of N-Char and N-Metal Biochars (wt %)

sample	500 °C	600 °C	700 °C	800 °C	900 °C
N-char	20.3 ± 0.2	17.9 + 0.2	17.5 ± 0.4	16.8 ± 0.3	15.5 ± 0.6
Mg-char				34.0 ± 0.3	
Mg-N-char				30.1 ± 0.4	
Ca-N-char				32.5 ± 0.9	
Fe-N-char				29.8 ± 0.4	

Table 2. Elemental Content of N-Doped Biochars from Cellulose (Dry Basis)

	dry basis				
samples	C (wt %)	H (wt %)	N (wt %)	O* (wt %)	Ash (wt %)
N-dopedchar_500	86.6 ± 0.4	3.1 ± 0.03	7.4 ± 0.1	2.9 ± 0.2	<0.1
N-dopedchar_600	87.5 ± 0.5	2.2 ± 0.01	7.8 ± 0.02	2.6 ± 0.2	<0.1
N-dopedchar_700	85.4 ± 0.5	1.2 ± 0.01	11.0 ± 0.05	2.4 ± 0.2	<0.1
N-dopedchar_800	84.7 ± 0.7	0.9 ± 0.01	12.5 ± 0.2	1.9 ± 0.3	<0.1
N-dopedchar_900	89.6 ± 0.7	0.6 ± 0.03	7.6 ± 0.1	2.1 ± 0.3	0.1

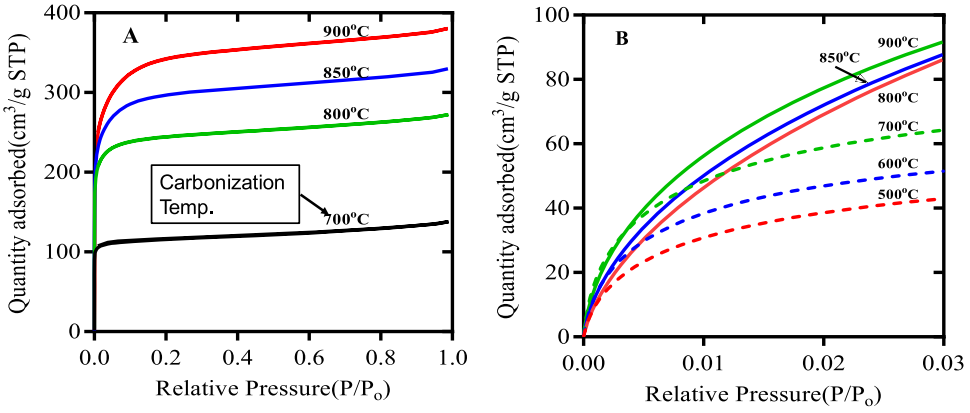

Figure 3. Adsorption isotherms of nitrogen-doped biochars produced from cellulose. (A) is the N_2 adsorption isotherm and (B) is the CO_2 adsorption isotherm.

as shown in Figure 2a,b; (ii) metal atom incorporation in the center of single- or double-point defect, as shown in Figure 2c.

To compare the DFT-based model systems of N-metal-doped carbon to the experimentally measured XPS spectra, the core-level energy shifts (E_{CLS}) of the metal 2p states were calculated according to

$$E_{CLS} = [E_{N-Me-Doped}(n_c - 1) - E_{N-Me-Doped}(n_c)] - [E_{bulk-Me}(n_c - 1) - E_{bulk-Me}(n_c)] \quad (3)$$

where n_c is the total number of core electrons in the system, $E_{N\text{-}Me\text{-}Doped}$ $(n_c - 1)$ is the total energy of the N-Metal-doped H-edge graphene model with a single core electron removed from the metal 2p state, $E_{N\text{-}Me\text{-}Doped}$ (n_c) is the total energy of the N-Metal-doped H-edge model with all core electrons present in the system, $E_{bulk\text{-}Me}$ $(n_c - 1)$ is the total energy of a bulk metal with a single core electron removed from a 2p state, and $E_{bulk\text{-}Me}(n_c)$ is the total energy of a bulk metal with all core electrons present in the system. The core-level binding energy shift was calculated using the final state approximation.[36] To obtain the core-level binding energies from the core-level binding energy shift values, we used the experimental binding of bulk metal (Magnesium) as the reference with a binding energy of 49.80 eV.[37]

3. RESULTS AND DISCUSSION

3.1. Biochar Yield. Table 1 presents the biochar yield of N-chars and N-metal biochars. The yield of N-char decreased with increasing temperature due to the loss of volatiles by the pyrolysis reactions, as expected.[37] The N-metal biochars present a higher yield than the N-chars because of the impregnated metal content in these biochars.

3.2. Characterization of N-Doped Biochars. Table 2 shows the elemental analysis of all N-doped biochars produced. Nitrogen content in the samples generally increased with processing temperature. The greatest nitrogen content appears at a temperature of 800 °C (12.5 wt %) (Table 2). The C, H, and O contents in the char decrease with temperature. If we multiply the yield of char reported in Table 1 by the content of the elements reported in Table 2, it is possible to explain these trends. Effectively, the quantity of C gradually decreases from 17.57 wt % at 500 °C to 13.88 wt % at 900 °C. The reduction in the content of C can be explained by the cleavage of some weak bridges between small polyaromatic structures that could lead to the removal of small polyaromatic rings. In the case of H, it gradually decreased from 2.7 wt % at 500 °C to 0.53 wt %. The hydrogen is removed as part of the removed small polyaromatic rings and during the formation of a larger poly-condensed ring system. The amount of N, on the other hand, remains almost constant at 500 and 600 °C and then increases rapidly at 700 and 800 °C. This increase can be

https://doi.org/10.1021/acsomega.1c05718
ACS Omega 2022, 7, 14490−14504

Table 3. Surface Area (Sa) and Pore Volume (PV) of N-Doped Biochars from Cellulose

sample	Sa_{N2} (m^2 g^{-1})	Sa_{CO2} (m^2 g^{-1})	PV_{micro} (cm^3 g^{-1})	PV_{meso} (cm^3 g^{-1})	PV_{total} (cm^3 g^{-1})
N-dopedchar_500		331.7	0.13		
N-dopedchar_600		386.2	0.15		
N-dopedchar_700	453.2	470.9	0.19	0.02	0.21
N-dopedchar_800	934.1	761.0	0.30	0.12	0.42
N-dopedchar_850	1169.9	764.2	0.31	0.20	0.51
N-dopedchar_900	1314.8	793.4	0.32	0.27	0.59

Table 4. Elemental Composition (wt %) of Metal-N-Doped Biochar Derived from Cellulose Produced at 800 °C[a]

	dry basis						
samples	C	H	N	O	VC	FC	Ash
N-Char	84.7 ± 0.7	0.9 ± 0.0	12.5 ± 0.2	1.9 ± 0.2	10.4 ± 0.3	89.6 ± 0.3	0.0 ± 0.0
Mg-Char	65.8 ± 0.0	0.8 ± 0.1	0.2 ± 0.0	5.1 ± 0.0	4.4 ± 0.1	67.5 ± 0.7	28.1 ± 0.7
Mg-N-Char	51.5 ± 0.5	1.0 ± 0.0	15.5 ± 0.1	7.8 ± 0.2	14.7 ± 0.4	61.0 ± 0.3	24.2 ± 0.1
Ca-N-Char	62.1 ± 2.3	0.6 ± 0.0	12.9 ± 0.0	0.7 ± 0.1	12.4 ± 1.0	64.2 ± 0.4	23.4 ± 0.7
Fe-N-Char	69.0 ± 0.3	0.8 ± 0.0	8.8 ± 0.0	2.8 ± 0.1	13.6 ± 0.4	67.8 ± 0.3	18.6 ± 0.1

[a]Note C (wt %) +H (wt %) +N (wt %) +O (wt %) + Ash (wt %) = 100.

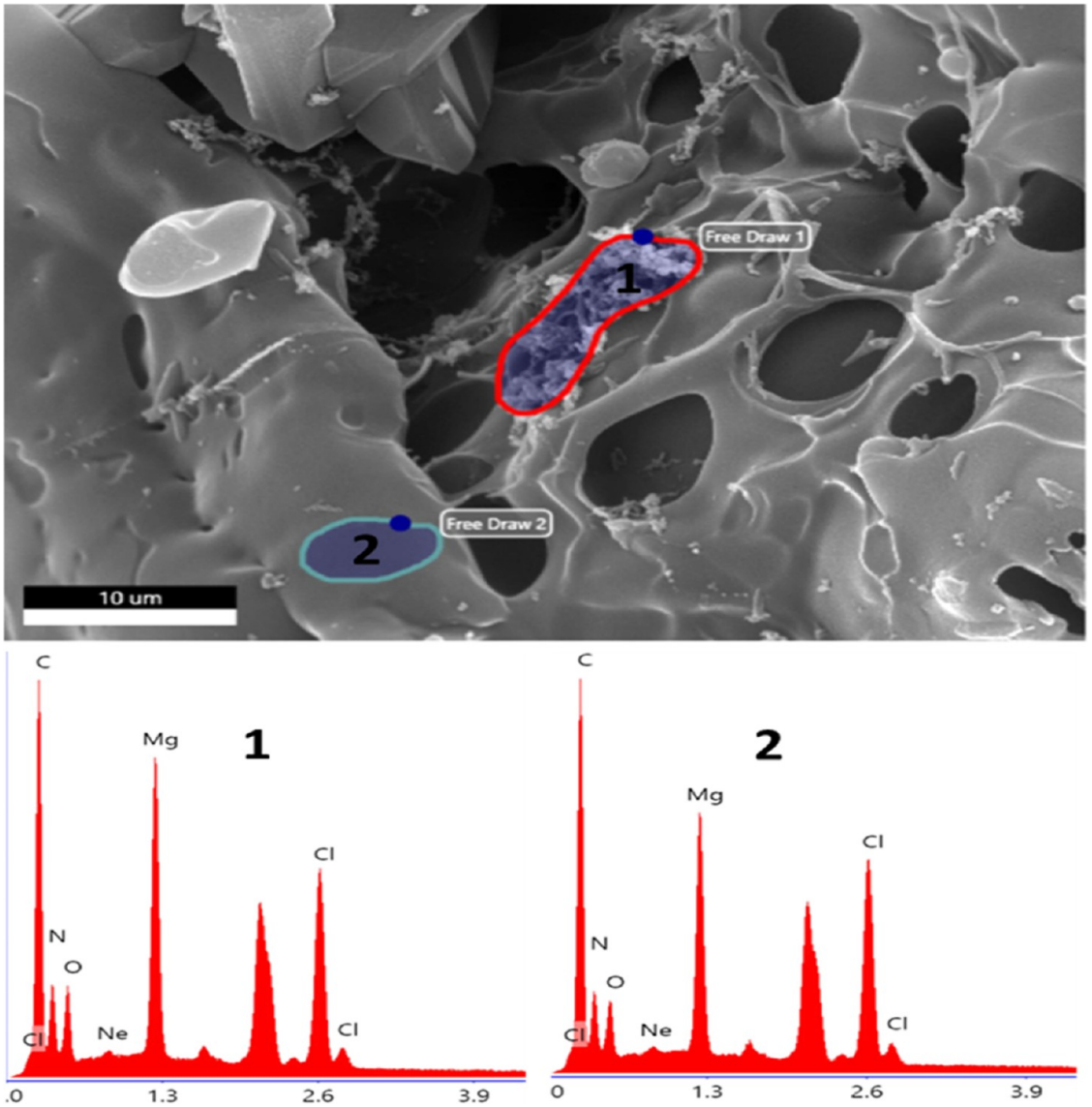

Figure 4. SEM-EDS images of N-Mg-Char in the two different regions. Region 1 shows the presence of crystals, while region 2 is smooth. The *X*- and *Y*-axes represent the energy of the X-rays emitted (measured in KeV) and the measured intensity in counts, respectively.

https://doi.org/10.1021/acsomega.1c05718
ACS Omega 2022, 7, 14490−14504

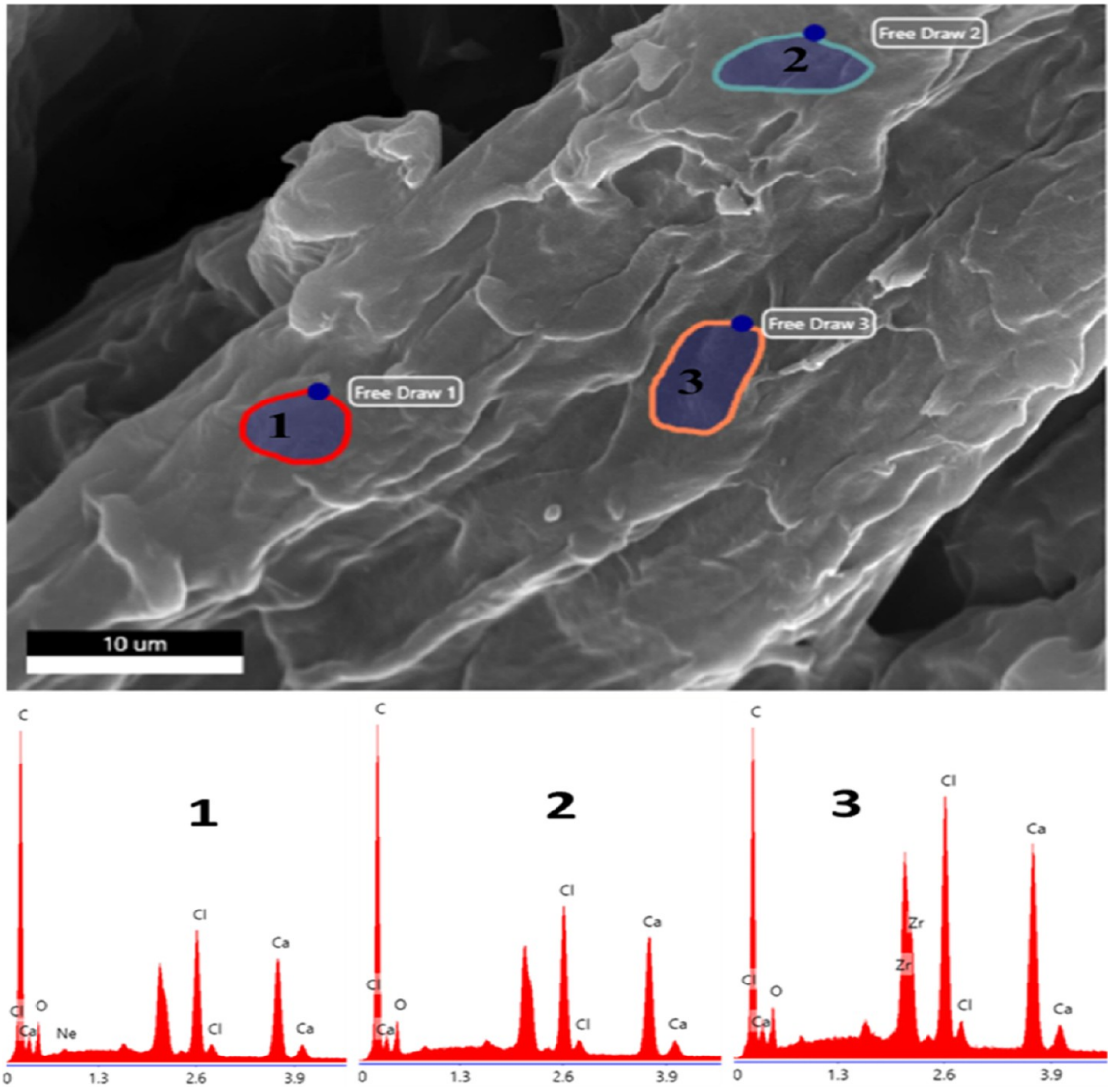

Figure 5. SEM-EDS images of N-Ca-Char. Region 1, 2, and 3 are regions without any Ca pores. The *X*- and *Y*-axes represent the energy of the X-rays emitted (measured in KeV) and the measured intensity in counts, respectively.

explained by the reaction between the polyaromatic rings and ammonia. At 900 °C, the N in polyaromatic structures seems to be thermally removed. Our group[17] recently examined the thermodynamic stability of nitrogen functionalities on different graphene and graphene using DFT-calculated Gibbs reaction energies. The most stable nitrogen functionality was pyridinic nitrogen, followed by graphitic nitrogen.

Figure 3 shows the CO_2 and N_2 adsorption isotherms for all of the N-doped biochars produced. A high surface area was achieved through ammonia-doping of cellulose biochar, with ammonia serving as an activating agent. The surface area analysis shows an increase in biochar surface area as the production temperatures are increased (500−900 °C). Note that specific surface area and pore volume are commonly determined by the measurement of physisorption of N_2 and/or CO_2. The maximum surface area (1314 m^2 g^{-1}, see Table 3) was achieved at 900 °C. The surface area measured in the range between 500 and 700 °C for chars produced under NH_3 was between 13 and 20% lower than the chars produced under N_2 reported by Smith et al.[38] It is worth mentioning that high surface area and pore volume are key biochar properties pertaining to water and nutrient cycling, microbial activity, and sorption of organic and inorganic compounds and gaseous pollutants.

3.3. Characterization of N-Metal-Doped Biochars. The elemental and proximate analysis of biochar doped with metals and nitrogen is presented in Table 4. The presence of metals had a significant influence on the carbonization process, namely by incorporating more nitrogen into the structure of the biochar. The presence of metals in chars has a catalytic effect on the formation of the nitrogen dopant.[39,40] This is particularly evident for the N-Mg-char, which contains 15.5 wt % nitrogen as compared to the 12.5 for its N-doped counterpart (Table 2). However, the carbon content decreases dramatically as compared to biochar without metals.

3.4. Morphological Structure of N-Mg (Ca, Fe) Biochars. Our SEM-EDS studies aimed to determine if metals were in the form of crystals on the surface of the chars or embedded within the matrix of the biochar. The results of these studies are shown in Figures 4−6 for N-Mg-Char, N-Ca-Char, and N-Fe-Char, respectively. Figure 4 shows the presence of both a smooth and a rough surface with some microcracks and shallow pores as a result of ammonia etching in the N-Mg-Char. Interestingly, metals were observed both in

https://doi.org/10.1021/acsomega.1c05718
ACS Omega 2022, 7, 14490−14504

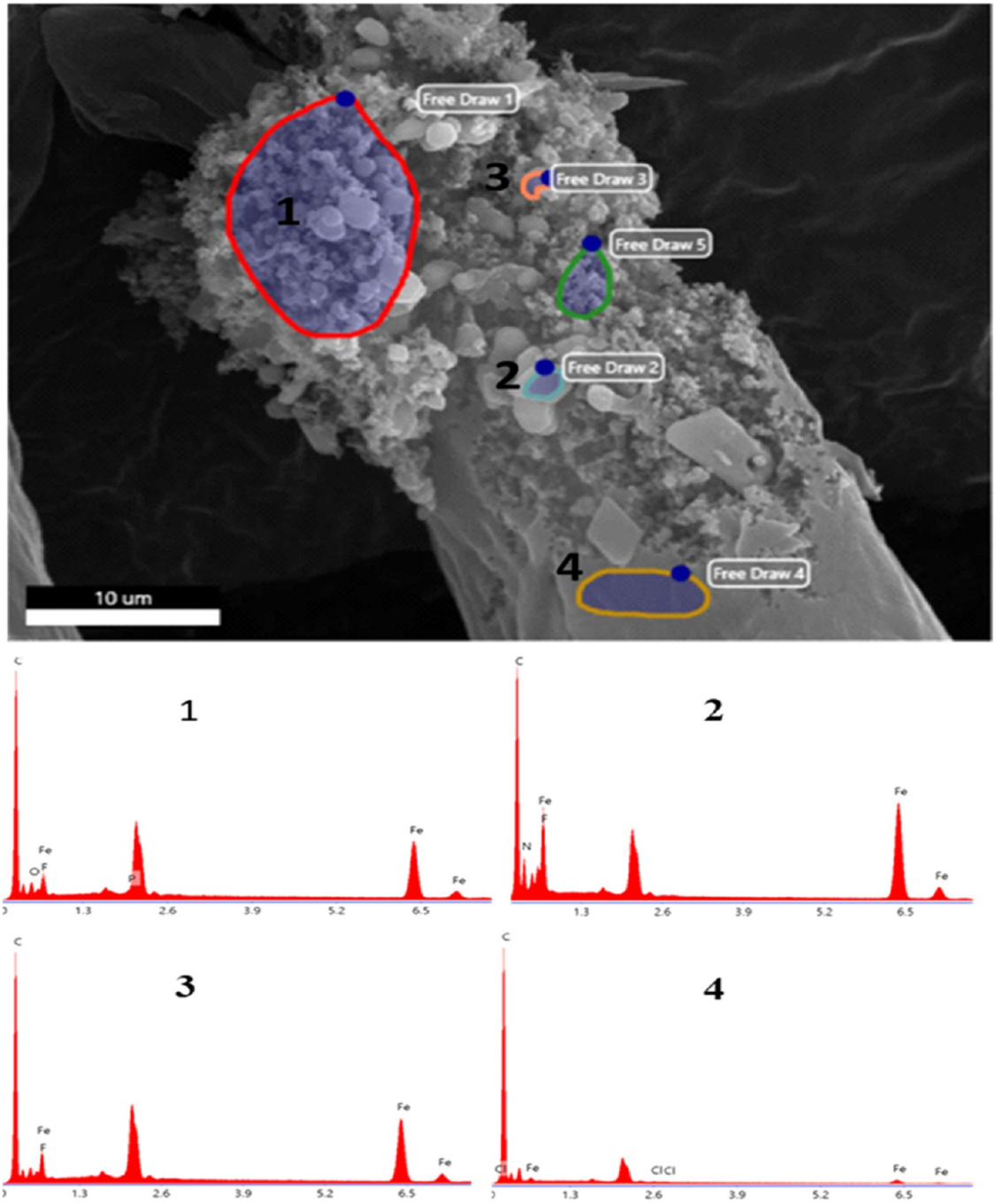

Figure 6. SEM-EDS images of N-Fe-Char. Only region 4 does not show any presence of crystals. Note that region 5 was not shown in the figure because it has similar spectra to regions 1, 2, and 3.

the form of crystals and embedded in the carbonaceous surface of the biochar. The EDS test results show Mg is present in both the crystals and the carbonaceous structure. Because only a small fraction of the surface is covered by crystals, we can hypothesize that most of the Mg is embedded within the carbon matrix.

Figure 5 shows the presence of a smooth surface rich in Ca without pores. Figure 6 shows the SEM-EDS of the N-Fe-doped biochar. It was observed that most of the Fe is in the form of crystals deposited on the surface. The content of Fe in the carbonaceous matrix (see Figure 6) is very low, with crystals making up the majority of iron in the char.

3.5. TEM and XRD. Figure 7 shows the TEM picture of the N-Mg-doped biochar. We do not see in this figure any evidence of the Mg forming nanocrystals. Although there are some crystals as indicated by the XRD peaks, EDS indicates most Mg is part of the polyaromatic carbon structure.

Figure 8 shows the TEM picture of the N-Ca-doped biochar. We can clearly see in the figure the presence of clusters or regions (likely nanocrystals in the range of 20−30 nm). This means that although the Ca can be found as part of the carbonaceous structure, it may also form nanoparticles.

Figure 9 shows the TEM of the N-Fe-doped biochars. Here, we observed the formation of very small nanoparticles of less than 5 nm in the carbon matrix.

https://doi.org/10.1021/acsomega.1c05718
ACS Omega 2022, 7, 14490−14504

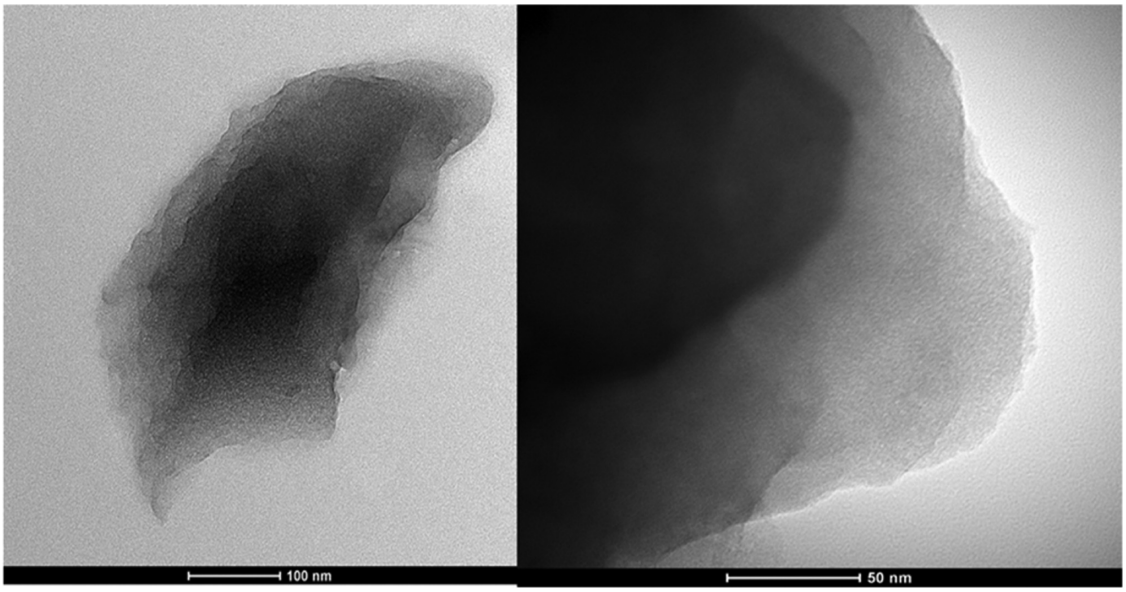

Figure 7. TEM of N-Mg-doped char.

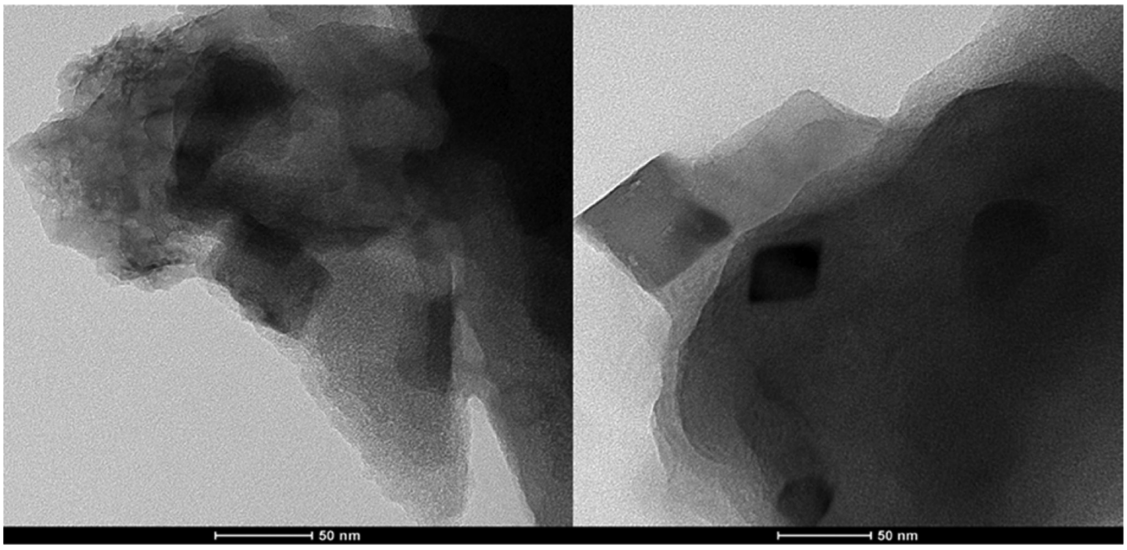

Figure 8. TEM of N-Ca-doped biochar.

Figure 10 shows the wide-angle XRD patterns of N-Mg, and N-Fe-biochar samples. The XRD data from N-Mg-Char confirm the presence of highly crystalline MgO particles. We found the presence of MgC_2N_2 with a crystallite size of about 9.5 nm. The broadness of the XRD peaks was used to calculate the crystalline size of MgO particles using the Scherrer equation. The results showed the presence of particles with a size between 9.5 nm and 50 nm (Table 5). The XRD of N-Fe-char only presents crystals of iron oxides with a crystallite size between 14.9 and 164.5 nm (Table 6).

3.6. High-Resolution XPS Spectra. The high-resolution spectra taken for each of N-Mg and N-Ca biochars are shown in Figure 11. The first figure (a) is the N 1*s* spectra, the middle figure (b) is the O 1*s*, while the third figure shows Mg 2*p* spectra (c). Here, it is worth noting that the Mg-Char presents a peak at 56 eV in the absence of nitrogen, but in the presence of nitrogen in the structure (N-Mg-Char), this peak is replaced by one at to 53.15 eV, in addition to an entirely new peak at about 49.85 eV is likely related to the bonding between N and Mg. The nitrogen dramatically affects the O 1*s* spectra as well, eliminating a peak that was present at 538 eV for char without N. These findings indicate that the nitrogen might have a stronger affinity toward the metal than the oxygen.

3.7. Computational Investigation of Site Stability and XPS Core-Level Binding Shifts (CLBES). To better understand the specific functionalities formed, we computationally quantified the stability of magnesium and calcium on internal and edge active sites, supported by various types of nitrogen functional groups. Below are the different types of structures that were tested.

The results (see Figure 16, this figure is based on data shown in Figures 12−15) indicate that the number of nitrogen functional groups and the configuration of those groups have a tremendous effect on metal binding stability. The internal active sites (metals held within the sheet by multiple nitrogen groups) turned out to be more favorable (since the adsorption energies are nearly all exothermic, i.e., negative) than the edge

https://doi.org/10.1021/acsomega.1c05718
ACS Omega 2022, 7, 14490−14504

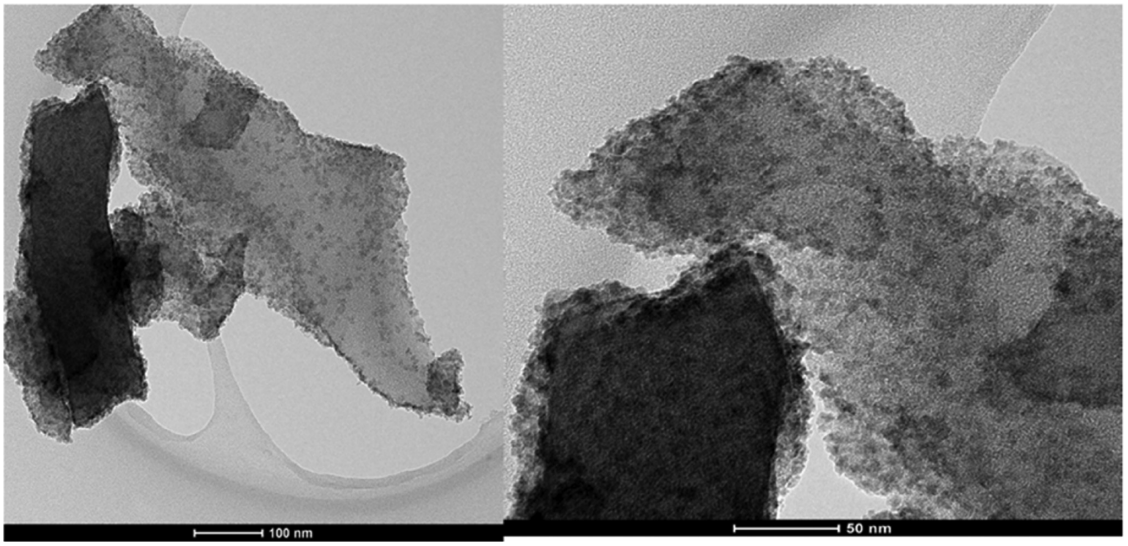

Figure 9. TEM picture of N-Fe-doped biochars.

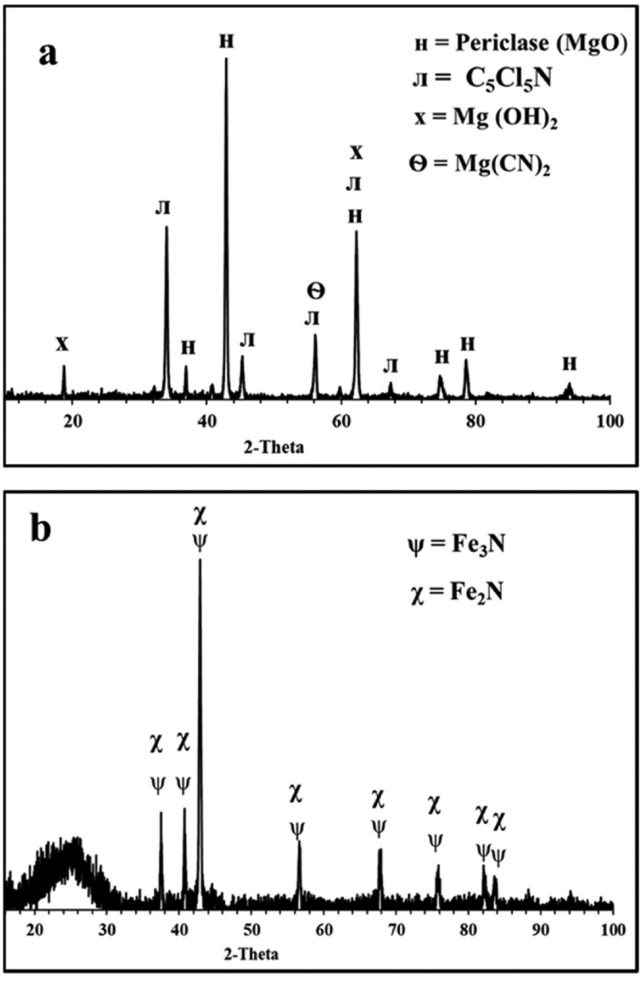

Figure 10. XRD of (a) N-Mg-Char and (b) N-Fe-Char.

active sites (since they are either highly endothermic, i.e., positive or only slightly exothermic).

As shown in Figure 16, the nitrogen species that bind to Mg/Ca have a noticeable effect on the adsorption energy. While the monofunctional group at the edge sites, with the corresponding structures as shown in Figures 13 and 15, does not bind favorably (since a positive value indicates an unfavorable adsorption), a pronounced effect is shown on the adsorption energy with a difunctional group at the edge, with pyridine and pyrrole. Figure 16 also explores the effect of increasing the pyridine/pyrrolic group on the stability of Mg/Ca within a di-and tri-vacancy defect. With these configurations, the adsorption of Mg/Ca becomes energetically favorable (since the adsorption energies are negative). However, a monovacancy region with three pyridine groups (see Figures 12c and 14c, $3P_6N$-Mg) coordinated to a Mg/Ca is not energetically stable due to steric effects. This structure becomes even less stable with the addition of two hydrogen atoms coordinated separately to nitrogen atoms, as shown in Figures 12a and 14a.

Table 5. Crystallite Size of the Correlated Phases in the N-Mg-Char

2θ [deg]	correlated phase(s)	crystallite size [nm]
18.68	C_5Cl_5N, Mg $(OH)_2$	9.45
33.93	C_5Cl_5N	28.04
36.79	MgO	20.12
45.24	C_5Cl_5N	31.3
55.99	C_5Cl_5N, Mg (C N)$_2$	9.56
62.14	MgO, C_5Cl_5N, Mg $(OH)_2$	21.37
67.19	C5CL5N_300K	18.68
74.65	MgO, C_5Cl_5N	21.59
78.6	MgO, C_5Cl_5N	50.19
93.85	MgO, C_5Cl_5N	17.63

Table 6. Crystallite Size of the Correlated Phases in the N-Fe-Char

2θ [deg]	correlated phase(s)	crystallite size [nm]
37.45	Fe_3N, Fe_2N	14.91
40.74	Fe_3N, Fe_2N	44.24
42.82	Fe_3N, Fe_2N	164.5
56.54	Fe_3N, Fe_2N	24.78
67.85	Fe_3N, Fe_2N	22.63
75.75	Fe_3N, Fe_2N	24.59
82.22	Fe_3N, Fe_2N	24.45
83.43	Fe_3N, Fe_2N	24.68

https://doi.org/10.1021/acsomega.1c05718
ACS Omega 2022, 7, 14490−14504

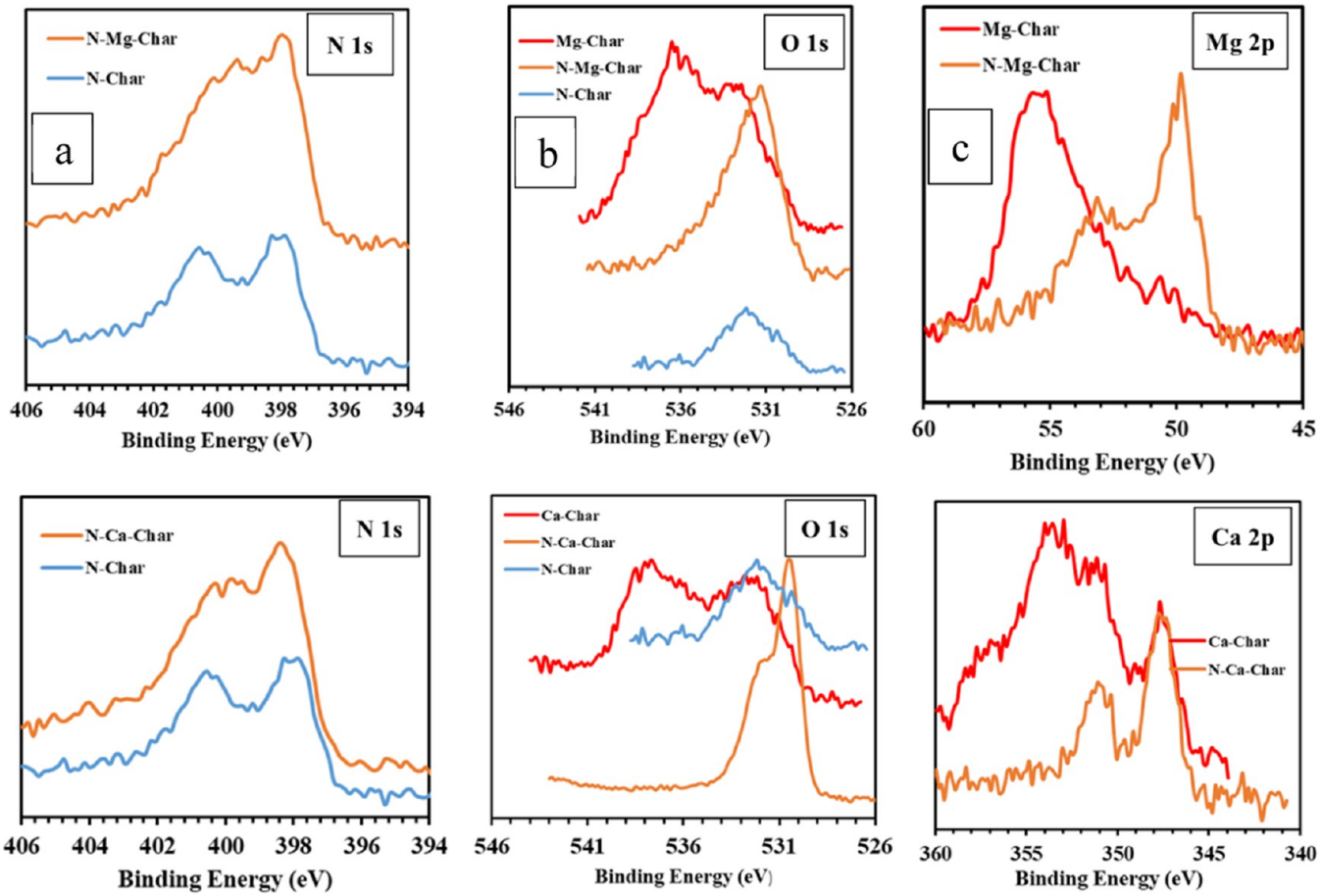

Figure 11. XPS spectra. The top figures consists of N-doped char, Mg-Char, and N-Mg-doped char. The bottom figures consist of N-doped char (a), Ca-Char (b), and N-Ca-doped biochar (c).

Table 7 depicts the core-level binding energies of the magnesium centers in structures, as shown in Figures 12 and 13. The goal of this study is to identify the type of structure in which the Mg could occupy the polyaromatic ring structure. Using bulk magnesium as the reference structure, the energy shifts were calculated based on eq 3. Note that there are significant shifts in the core-level binding energies for the $4P_5N$-Mg and the P_5N-Mg structures with corresponding core-level binding of energies 51.86 and 52.06 eV, respectively. These energies are closest to the observed peak occurring at higher energies (53.15 eV), as shown in Figure 11 for N-Mg-Char but do not seem close enough to explain it. Structures $4P_6N$-Mg, $3P_6N$-MgH_2, $3P_6N$-Mg, $2P_6N$-Mg, and $2P_5N$-Mg show energies that closely match the lower experimental binding energy peak (49.85 eV) (see Figure 11, N-Mg-Char). Of these, $4P_6N$-Mg represents the only structure with a favorable Mg adsorption energy, meaning it is likely responsible for the lower energy peak seen under the initial analysis.

However, it should also be noted that the results from this initial analysis do not necessarily transfer to the analysis of their use case. The presence of water is shown in Table 7 and Figure 17 to have both a strong adsorption on magnesium and a marked effect on its XPS binding energy. As such, these results should be interpreted with the associated uncertainty under the aqueous conditions in which they will be applied.

4. CONCLUSIONS

In the case of the N-Fe-doped biochar, we not only see the formation of large quantified of macro-crystals in the micrometer range size, but also observed the presence of nanocrystals (less than 5 nm). In the case of N-Ca-doped biochars, we see the formation of nanometer-size crystals (between 20 and 30 nm) and Ca-N structures embedded on the carbonaceous matrix. In the case of the N-Mg biochars, it seems that most of it is part of the polyaromatic ring structure. According to the adsorption energies computed, the edge active sites bind metals less favorably and might have the highest potential of binding to phosphate ions than the centered active sites. The XPS results clearly show an interaction between Mg and N in the polyaromatic ring system, resulting in pronounced Mg 2*p* core-level binding energy shifts. DFT-based calculations confirm that the shift in the Mg 2*p* core-level binding energy could be due to the formation of phthalocyanine-like structures and N-Mg complexes formed on the edges of the graphene sheet. In a nutshell, cellulose char doped with nitrogen and metals, such as Mg and Ca, could produce phthalocyanine-like structures; these structures are more stable and highly not favorable in terms of binding to phosphate ions. However, nitrogenated and metallic structures at the edges of the carbon network, per the DFT-based calculations, are less favorable structures, and we hypothesize they have the highest probability to bind to phosphate ions. The second part of this paper shows the results

https://doi.org/10.1021/acsomega.1c05718
ACS Omega 2022, 7, 14490−14504

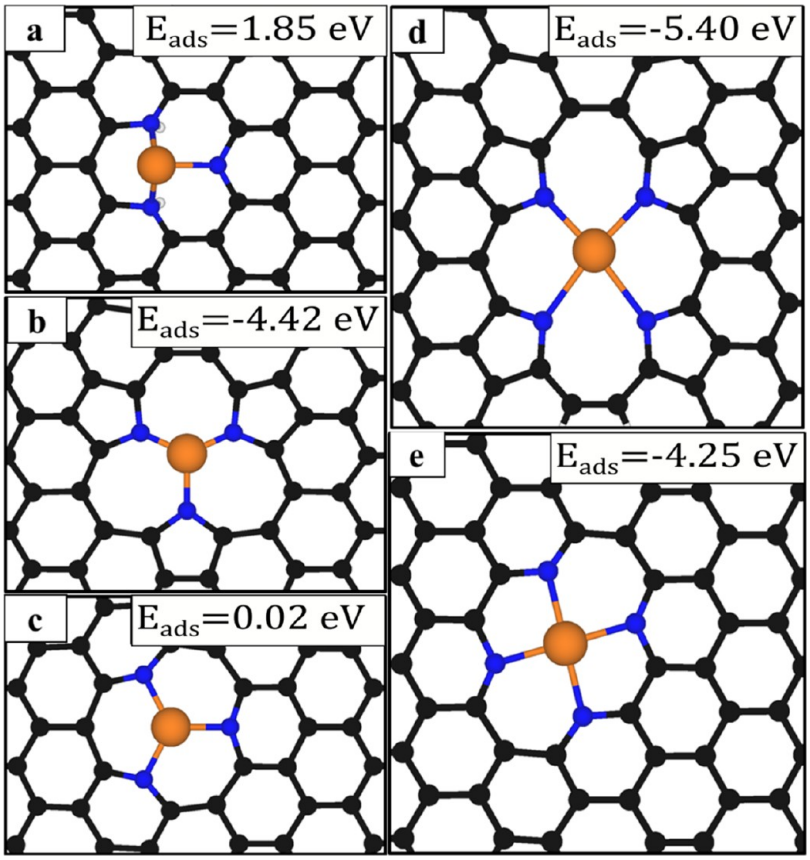

Figure 12. Molecular scheme of Mg-N-doped biochars within a graphene model structure with a (a) $3P_6N$-MgH_2, (b) $3P_5N$-Mg, (c) $3P_6N$-Mg, (d) $4P_5N$-Mg, and (e) $4P_6N$-Mg functionality, where the black, blue, white, and orange spheres represent carbon, nitrogen, hydrogen, and magnesium atoms, respectively.

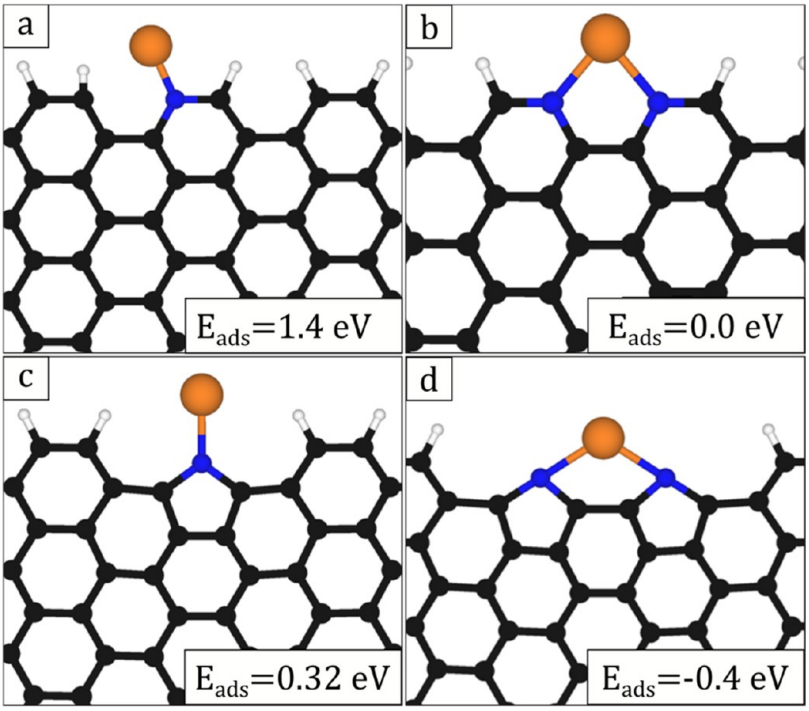

Figure 13. Magnesium adsorption energies at the edge of graphene with pyrrolic and pyridinic groups with a (a) P_6N-Mg, (b) $2P_6N$-Mg, (c) P_5N-Mg, and (d) $2P_5N$-Mg functionality. The sphere legend is as given in Figure 12.

https://doi.org/10.1021/acsomega.1c05718
ACS Omega 2022, 7, 14490−14504

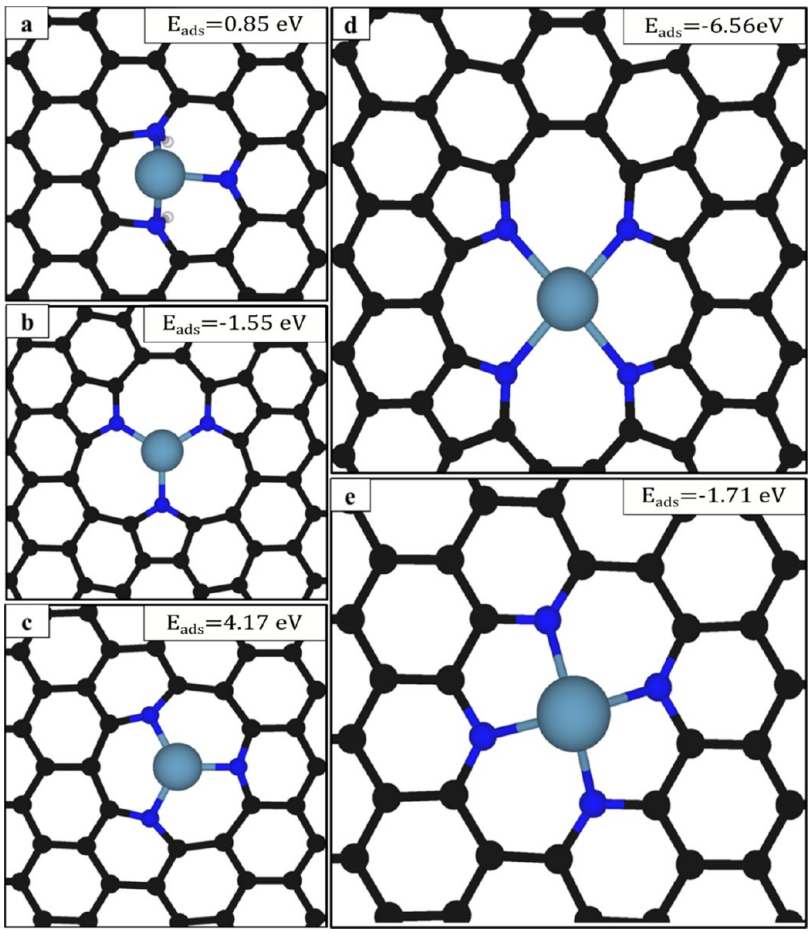

Figure 14. Calcium adsorption energies at the center of graphene with pyrrolic and pyridine groups with a (a) $3P_6N$-MgH_2, (b) $3P_5N$-Mg, (c) $3P_6N$-Mg, (d) $4P_5N$-Mg, and (e) $4P_6N$-Mg functionality, where the black, blue, blue-green, and white spheres represent carbon, nitrogen, calcium, and hydrogen atoms, respectively.

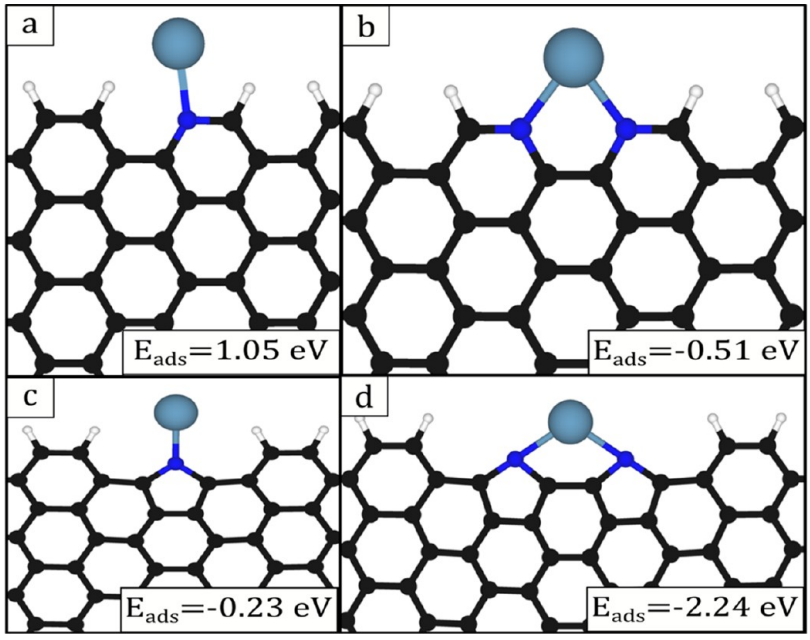

Figure 15. Calcium adsorption energies at the edge of graphene with pyrrolic and pyridinic groups with a (a) P_6N-Mg, (b) $2P_6N$-Mg, (c) P_5N-Mg, and (d) $2P_5N$-Mg functionality. There sphere legend is as given in Figure 14.

https://doi.org/10.1021/acsomega.1c05718
ACS Omega 2022, 7, 14490−14504

Table 7. CLBE Shifts of N-Mg-Model Coordination in a Graphene Sheet

structures	CLBEs	computed binding energy (eV)	experimental (eV) ref 36
		N-Mg-Structures (Centered Active Sites)	
$3P_6N$-MgH_2	1.03	50.83	
$3P_5N$-Mg	−0.68	49.12	
$3P_6N$-Mg	−0.39	49.41	
$4P_5N$-Mg	2.06	51.86	
$4P_6N$-Mg	−0.36	49.44	
$4P_6N$-Mg-H_2O	0.02	49.82	49.80
		N-Mg-Structures (Edge Active Sites)	
$2P_6N$-Mg	−0.11	49.69	
P_5N-Mg	2.26	52.06	
$2P_5N$-Mg	1.34	51.14	

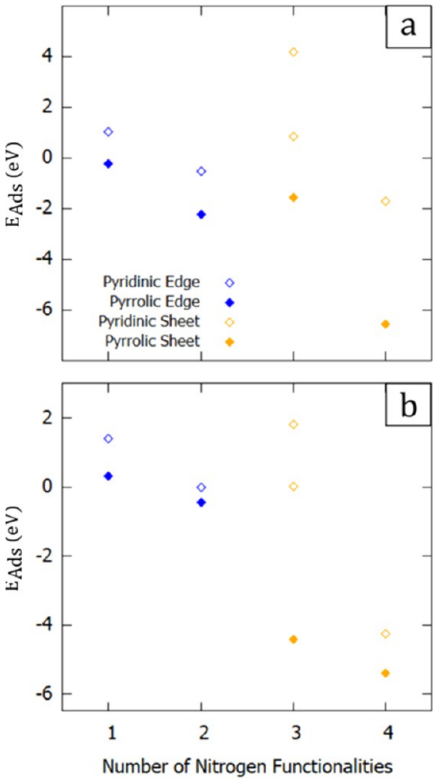

Figure 16. Adsorption energies of Mg and Ca with increasing number of pyridine and pyrrolic functional groups. (a) N-Mg-doped sheet and (b) N-Ca-doped sheet.

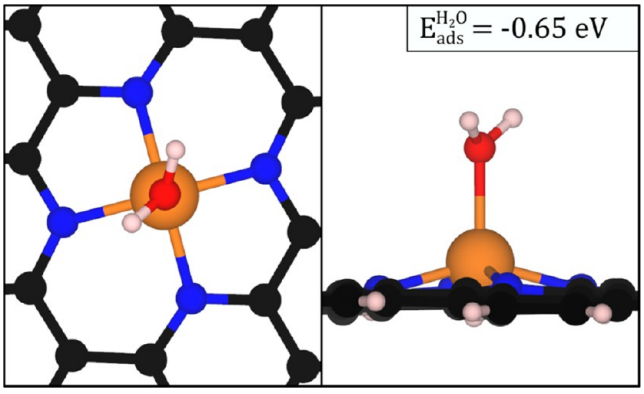

Figure 17. Adsorption structure and energy of free water onto the $4P_6N$-Mg functionality. The sphere legend is as given in Figure 12, with the addition of red spheres to represent oxygen.

of the phosphate adsorption with the characterized char in this paper.

AUTHOR INFORMATION

Corresponding Authors

Jean-Sabin McEwen − *Department of Biological Systems Engineering, Washington State University, Pullman, Washington 99164, United States; Gene and Linda Voiland School of Chemical Engineering and Bioengineering, Pullman, Washington 99164, United States; Department of Physics and Astronomy and Department of Chemistry, Washington State University, Pullman, Washington 99164, United States; Institute for Integrated Catalysis, Pacific Northwest National Laboratory, Richland, Washington 99352, United States;* orcid.org/0000-0003-0931-4869; Phone: 509-335-8580; Email: js.mcewen@wsu.edu

Manuel Garcia-Perez − *Department of Biological Systems Engineering, Washington State University, Pullman, Washington 99164, United States;* orcid.org/0000-0002-9386-2632; Phone: 509-372-7461; Email: mgarcia-perez@wsu.edu

Authors

Michael Ayiania − *Department of Biological Systems Engineering, Washington State University, Pullman, Washington 99164, United States*

Aidan Garcia − *Gene and Linda Voiland School of Chemical Engineering and Bioengineering, Pullman, Washington 99164, United States*

Sohrab Haghighi Mood − *Department of Biological Systems Engineering, Washington State University, Pullman, Washington 99164, United States*

Complete contact information is available at: https://pubs.acs.org/10.1021/acsomega.1c05718

Notes

The authors declare no competing financial interest.

ACKNOWLEDGMENTS

This work was supported by the National Science Foundation under Contract No. CBET-1703052. The authors would like to thank the Murdock Charitable Trust Fund for its financial support in upgrading our existing XPS instrument. Dr. Garcia-Perez would like to thank the Washington State Applied Bioenergy program (Appendix A) and the Sun Grant Initiative (Federal USDA/NIFA Award: 2014-38502-22598) for the financial support provided. This research used resources from the Center for Institutional Research Computing at Wash-

https://doi.org/10.1021/acsomega.1c05718
ACS Omega 2022, 7, 14490−14504

ington State University. This work was partially funded by the Joint Center for Deployment and Research in Earth Abundant Materials (JCDREAM) in Washington State. PNNL is a multiprogram national laboratory operated for the US DOE by Battelle.

REFERENCES

(1) Wang, X.; Li, X.; Zhang, L.; Yoon, Y.; Weber, P. K.; Wang, H.; Guo, J.; Dai, H. N-doping of graphene through electrothermal reactions with ammonia. *Science* **2009**, *324*, 768−771.
(2) Deng, D.; Pan, X.; Yu, L.; Cui, Y.; Jiang, Y.; Qi, J.; Li, W.-X.; Fu, Q.; Ma, X.; Xue, Q.; Sun, G.; Bao, X. Toward N-doped graphene via solvothermal synthesis. *Chem. Mater.* **2011**, *23*, 1188−1193.
(3) Cheng, Y.; Zhao, S.; Li, H.; He, S.; Veder, J.-P.; Johannessen, B.; Xiao, J.; Lu, S.; Pan, J.; Chisholm, M. F.; Yang, S.-Z.; Liu, C.; Chen, J. G.; Jiang, S. P. Unsaturated edge-anchored Ni single atoms on porous microwave exfoliated graphene oxide for electrochemical CO_2. *Appl. Catal., B* **2019**, *243*, 294−303.
(4) Geng, D.; Chen, Y.; Chen, Y.; Li, Y.; Li, R.; Sun, X.; Ye, S.; Knights, S. High oxygen-reduction activity and durability of nitrogen-doped graphene. *Energy Environ. Sci.* **2011**, *4*, 760−764.
(5) Imran Jafri, R.; Rajalakshmi, N.; Ramaprabhu, S. Nitrogen doped graphene nanoplatelets as catalyst support for oxygen reduction reaction in proton exchange membrane fuel cell. *J. Mater. Chem.* **2010**, *20*, 7114−7117.
(6) Adib, F.; Bagreev, A.; Bandosz, T. J. Adsorption/oxidation of hydrogen sulfide on nitrogen-containing activated carbons. *Langmuir* **2000**, *16*, 1980−1986.
(7) Chen, H.; Sun, F.; Wang, J.; Li, W.; Qiao, W.; Ling, L.; Long, D. Nitrogen doping effects on the physical and chemical properties of mesoporous carbons. *J. Phys. Chem. C* **2013**, *117*, 8318−8328.
(8) Nandi, M.; Okada, K.; Dutta, A.; Bhaumik, A.; Maruyama, J.; Derks, D.; Uyama, H. Unprecedented CO_2 uptake over highly porous N-doped activated carbon monoliths prepared by physical activation. *Chem. Commun.* **2012**, *48*, 10283−10285.
(9) Yao, Y.; Gao, B.; Chen, J.; Yang, L. Engineered biochar reclaiming phosphate from aqueous solutions: Mechanisms and potential application as a slow-release fertilizer. *Environ. Sci. Technol.* **2013**, *47*, 8700−8708.
(10) Alfarra, A.; Frackowiak, E.; Beguin, F. Mechanism of lithium electrosorption by activated carbons. *Electrochim. Acta* **2002**, *47*, 1545−1553.
(11) Chen, P.; Xiao, T.-Y.; Qian, Y.-H.; Li, S.-S.; Yu, S.-H. A Nitrogen-Doped Graphene/Carbon Nanotube Nanocomposite with Synergistically Enhanced Electrochemical Activity. *Adv. Mater.* **2013**, *25*, 3192−3196.
(12) Frackowiak, E.; Béguin, F. Electrochemical storage of energy in carbon nanotubes and nanostructured carbons. *Carbon* **2002**, *40*, 1775−1787.
(13) Wu, G.; More, K. L.; Johnston, C. M.; Zelenay, P. High-performance electrocatalysts for oxygen reduction derived from polyaniline, iron, and cobalt. *Science* **2011**, *332*, 443−447.
(14) Yu, D.; Nagelli, E.; Du, F.; Dai, L. Metal-free carbon nanomaterials become more active than metal catalysts and last longer. *J. Phys. Chem. Lett.* **2010**, *1*, 2165−2173.
(15) Zhang, L.; Zhang, J.; Wilkinson, D. P.; Wang, H. Progress in preparation of non-noble electrocatalysts for PEM fuel cell reactions. *J. Power Sources* **2006**, *156*, 171−182.
(16) Mood, S. H.; Ayiania, M.; Jefferson-Milan, Y.; Garcia-Perez, M. Nitrogen doped char from anaerobically digested fiber for phosphate removal in aqueous solutions. *Chemosphere* **2020**, *240*, No. 124889.
(17) Ayiania, M.; Hensley, A. J. R.; Groden, K.; Garcia-Perez, M.; McEwen, J.-S. Thermodynamic stability of nitrogen functionalities and defects in graphene and graphene nanoribbons from first principles. *Carbon* **2019**, *152*, 715−726.
(18) Ayiania, M.; Smith, M.; Hensley, A. J. R.; Scudiero, L.; McEwen, J.-S.; Garcia-Perez, M. Deconvoluting the XPS spectra for nitrogen-doped chars: An analysis from first principles. *Carbon* **2020**, *162*, 528−544.
(19) Ayiania, M.; Weiss-Hortala, E.; Smith, M.; McEwen, J.-S.; Garcia-Perez, M. Microstructural analysis of nitrogen-doped char by Raman spectroscopy: Raman shift analysis from first principles. *Carbon* **2020**, *167*, 559−574.
(20) Krasheninnikov, A. V.; Nieminen, R. M. Attractive interaction between transition-metal atom impurities and vacancies in graphene: a first-principles study. *Theor. Chem. Acc.* **2011**, *129*, 625−630.
(21) Bertier, P.; Schweinar, K.; Stanjek, H.; Ghanizadeh, A.; Clarkson, C. R.; Busch, A.; Kampman, N.; Prinz, D.; Amann-Hildenbrand, A.; Krooss, B. M.; Pipich, V.; Schäfer, T.; Dohrmann, R.; Greenwell, H. C. On the Use and Abuse of N2 Physisorption for the Characterization of the Pore Structure of Shales. *Filling the Gaps − from Microscopic Pore Structures to Transport Properties in Shales*; Clay Minerals Society, 2016; Vol. *21*.
(22) Dubinin, M. M. The equation of the characteristic curve of activated charcoal. *Proc. USSR Acad. Sci.* **1947**, *55*, 327−329.
(23) Dubinin, M. M.; Zaverina, E. D.; Radushkevich, L. V. Sorption and structure of active carbons I. Adsorption of organic vapors. *Zh. Fiz. Khim.* **1947**, *21*, 1351−1362.
(24) Kresse, G.; Furthmüller, J. Efficiency of ab-initio total energy calculations for metals and semiconductors using a plane-wave basis set. *Comput. Mater. Sci.* **1996**, *6*, 15−50.
(25) Kresse, G.; Furthmüller, J. Efficient iterative schemes for ab initio total-energy calculations using a plane-wave basis set. *Phys. Rev. B: Condens. Matter Mater. Phys.* **1996**, *54*, 11169−11186.
(26) Kresse, G.; Hafner, J. Ab initio molecular dynamics for liquid metals. *Phys. Rev. B: Condens. Matter Mater. Phys.* **1993**, *47*, 558−561.
(27) Hensley, A. J. R.; Zhang, J.; Vinçon, I.; Pereira Hernandez, X.; Tranca, D.; Seifert, G.; McEwen, J.-S.; Wang, Y. Mechanistic understanding of methanol carbonylation: Interfacing homogeneous and heterogeneous catalysis via carbon supported IrLa. *J. Catal.* **2018**, *361*, 414−422.
(28) Kresse, G.; Joubert, D. From ultrasoft pseudopotentials to the projector augmented-wave method. *Phys. Rev. B: Condens. Matter Mater. Phys.* **1999**, *59*, 1758−1775.
(29) Perdew, J. P.; Burke, K.; Ernzerhof, M. Generalized gradient approximation made simple. *Phys. Rev. Lett.* **1996**, *77*, 3865−3868.
(30) Gerber, I. C.; Krasheninnikov, A. V.; Foster, A. S.; Nieminen, R. M. A first-principles study on magnetic coupling between carbon adatoms on graphene. *New J. Phys.* **2010**, *12*, No. 113021.
(31) Isvoranu, C.; Åhlund, J.; Wang, B.; Ataman, E.; Mårtensson, N.; Puglia, C.; Andersen, J. N.; Bocquet, M.-L.; Schnadt, J. Electron spectroscopy study of the initial stages of iron phthalocyanine growth on highly oriented pyrolitic graphite. *J. Chem. Phys.* **2009**, *131*, No. 214709.
(32) Mehmood, F.; Pachter, R.; Lu, W.; Boeckl, J. J. Adsorption and diffusion of oxygen on single-layer graphene with topological defects. *J. Phys. Chem. C* **2013**, *117*, 10366−10374.
(33) Pulido, A.; Boronat, M.; Corma, A. Theoretical investigation of gold clusters supported on graphene sheets. *New J. Chem.* **2011**, *35*, 2153−2161.
(34) Hou, Z.; Wang, X.; Ikeda, T.; Terakura, K.; Oshima, M.; Kakimoto, M.-a.; Miyata, S. Interplay between nitrogen dopants and native point defects in graphene. *Phys. Rev. B: Condens. Matter Mater. Phys.* **2012**, *85*, No. 165439.
(35) Momma, K.; Izumi, F. VESTA 3 for three-dimensional visualization of crystal, volumetric and morphology data. *J. Appl. Crystallogr.* **2011**, *44*, 1272−1276.
(36) Köhler, L.; Kresse, G. Density functional study of CO on Rh(111). *Phys. Rev. B: Condens. Matter Mater. Phys.* **2004**, *70*, No. 165405.
(37) Steiner, P.; Höchst, H.; Hüfner, S. XPS investigation of simple metals. *Z. Phys. B: Condens. Matter* **1978**, *30*, 129−143.
(38) Smith, M.; Pecha, B.; Helms, G.; Scudiero, L.; Garcia-Perez, M. Chemical and morphological evaluation of chars produced from primary biomass constituents: cellulose, xylan and lignin. *Biomass and Bioenergy* **2017**, *104*, 17−35.

https://doi.org/10.1021/acsomega.1c05718
ACS Omega 2022, 7, 14490−14504

(39) Wan, Z.; Sun, Y.; Tsang, D. C. W.; Khan, E.; Yip, A. C. K.; Ng, Y. H.; Rinklebe, J.; Ok, Y. S. Customised fabrication of nitrogen-doped biochar for environmental and energy applications. *Chem. Eng. J.* **2020**, *401*, No. 126136.
(40) Haghighi Mood, S.; Ayiania, M.; Cao, H.; Marin-Flores, O.; Milan, Y. J.; Garcia-Perez, M. Nitrogen and magnesium Co-doped biochar for phosphate adsorption. *Biomass Conv. Bioref.* **2021**, DOI: 10.1007/s13399-021-01404-1.

https://doi.org/10.1021/acsomega.1c05718
ACS Omega 2022, 7, 14490−14504